Journal of Electrochemistry

Volume 28
Issue 10 *Special Issue on Water Electrolysis for Hydrogen Production (Ⅱ)*

2022-10-28

Catalytic Effect of Disordered Ru-O Configurations for Electrochemical Hydrogen Evolution

Xue Sun

Ya-Jie Song

Ren-Long Li

Jia-Jun Wang
1. MIIT Key Laboratory of Critical Materials Technology for New Energy Conversion and Storage, Harbin Institute of Technology, Harbin, 150001, China;2. Chongqing Research Institute of HIT, Chongqing 401135, P. R. China;, jiajunhit@hit.edu.cn

Recommended Citation
Xue Sun, Ya-Jie Song, Ren-Long Li, Jia-Jun Wang. Catalytic Effect of Disordered Ru-O Configurations for Electrochemical Hydrogen Evolution[J]. *Journal of Electrochemistry*, 2022 , 28(10): 2214011.
DOI: 10.13208/j.electrochem.2214011
Available at: https://jelectrochem.xmu.edu.cn/journal/vol28/iss10/3

电 化 学
J. Electrochem. 2022, 28(10), 2214011 (1 of 11)

[Article] DOI: 10.13208/j.electrochem.2214011 Http://electrochem.xmu.edu.cn

Catalytic Effect Of Disordered Ru-O Configurations for Electrochemical Hydrogen Evolution

Xue Sun[1,2], Ya-Jie Song[1,2], Ren-Long Li[1], Jia-Jun Wang[1,2*]

(*1. MIIT Key Laboratory of Critical Materials Technology for New Energy Conversion and Storage, Harbin Institute of Technology, Harbin, 150001, China; 2. Chongqing Research Institute of HIT, Chongqing 401135, P. R. China.*)

Abstract: Phase engineering is considered as an effective method for modulating the electronic structure and catalytic activity of catalysts. The disordered conformation of amorphous materials allows flexible reforming of the surface electronic structure, showing their attractiveness as catalysts for hydrogen evolution reaction (HER). Herein, we designed and developed an amorphous ruthenium dioxide (a-RuO_2) catalyst with a disordered Ru-O configuration. The conformational relationship between Ru-O ordering and HER performance is established by combining advanced electron microscopic techniques with detailed electrochemical tests. Specifically, the disordered Ru-O coordination significantly enhanced the HER catalytic activity in both acidic and alkaline media, ultimately leading to HER performance of a-RuO_2 approaching that of commercial Pt/C with higher economics. In addition, a-RuO_2 exhibited excellent stability after 10 h current-time (*i-t*) testing at 10 mA·cm^{-2}. Further theoretical simulations showed that the lowered d-band center and optimized electron transport of a-RuO_2 modulated the adsorption strength of the active site to the intermediate reactants, promoting HER kinetics. This work provides a new perspective for exploring highly active HER catalysts through phase engineering.

Key words: phase engineering; hydrogen evolution reaction; amorphous catalyst; electronic structure

1 Introduction

As a new energy source that is clean, efficient, safe and sustainable, hydrogen energy is considered the most promising alternative energy source to fossil fuels and a strategic energy development direction for humankind[1-3]. Electrocatalytic HER represents a sustainable route to hydrogen production. Although platinum (Pt)-based catalysts can significantly reduce HER overpotential, their high cost and low reservoir abundance limit their practical application[4]. In addition, transition metals tend to be dissolved at high current densities, resulting in poor stability of transition metal-based catalysts[5]. In recent years, ruthenium (Ru) has stimulated great interest among researchers with its lowest price among Pt group metals, good catalytic properties and high resistance to corrosion in alkaline and neutral media[6, 7]. However, the current HER activity of Ru-based catalysts still has a large gap compared with Pt.

Over the past decades, various methods such as crystallographic surface modulation, alloying, heteroatom doping, and interfacial defect engineering have proven effective strategies to enhance the HER performance of Ru-based catalysts[8-10]. However, the catalysts modified by the above strategies are still crystalline materials, and their catalytic performance is limited by the fact that crystals can only undergo surface catalysis. Although the conversion efficiency on a geometric-area basis can be improved by increasing the catalyst loading or the exposed surface area,

Cite as: Sun X, Song Y J, Li R L, Wang J J. Catalytic effect of disordered Ru-O configurations for electrochemical hydrogen evolution. *J. Electroche*m., 2022, 28(10): 2214011.

Received: 2022-07-09, Revised: 2022-08-28. *Corresponding author, Tel: (86-451)86412114, E-mail: jiajunhit@hit.edu.cn

this approach leads to an increase in the electrode series resistance and thus a decrease in mass transfer. In addition, the highly active crystalline surfaces of crystalline Ru-based catalysts (e.g., RuO_2) are highly susceptible to reforming damage during long-term catalytic reactions, resulting in a limited catalytic lifetime[11, 12].

Recently, research on amorphous materials for HER catalysts has been emerging[13-15]. Amorphous electrocatalysts have a distinct identity of short-range order and long-range disorder, and reveal individual physical and chemical capabilities to their crystalline materials, contributing to remarkable catalytic performance. For the past few years, amorphous catalysts have become more attractive owing to their outstanding catalytic performance in electrochemical hydrogen evolution. For example, Yu's group verified that the amorphous NiFeMo materials are better than the most ordinary crystalline materials in solutions[13]. Wang and co-workers confirmed that the amorphous glassy electrocatalyst (MG) is superior to impulse HER than crystalline materials[14]. Xie et al. reported an amorphous metal substitution, verifying the catalyst to achieve a low onset potential during HER[15].

Compared with crystalline materials, sub-stable amorphous materials exhibit numerous excellent properties. In most cases, the effectiveness of catalytic systems can be enhanced by either increasing the number of active sites or intrinsic activity. Amorphous materials combine these two strategies. The flexibility of amorphous materials allows dynamic surface reconstruction of active sites to meet any geometry required for HER, enhancing the number of active sites[16]. On the other hand, amorphous materials contain a variety of low-coordination sites, allowing for suitable acceptors for both *H and *OH. In addition, the self-healing properties of amorphous catalysts allow for more excellent corrosion resistance[17]. On this basis, the amorphization of RuO_2 may bring new development opportunities for this traditional material. However, the synthesis and regulatory mechanisms of amorphous RuO_2 (named a-RuO_2) electrocatalysts have been explored to a limited extent.

Herein, we developed a-RuO_2 catalysts with disordered structure by low-temperature one-step thermal treatment. Density functional theory (DFT) calculations show that the disordered Ru-O configuration lowers the energy barrier for the decomposition of H_2O to H*/OH* while allowing the H* adsorbed on the a-RuO_2 surface to rapidly recombine to form H_2, resulting in fast acidic and alkaline HER kinetics. As a result, a-RuO_2 achieves excellent HER performance—an overpotential of 110 mV at a current density of 10 $mA \cdot cm^{-2}$ in alkaline media and 85 mV in acidic media. Our work provides a fundamental understanding of crystal engineering and hydrogen precipitation properties.

2 Experimental Section

2.1 Materials

Commercial crystalline RuO_2 (c-RuO_2), ruthenium chloride hydrate ($RuCl_3 \cdot xH_2O$, 99%), and potassium bromide (KBr, 99.9%) were purchased from Aladdin Reagent Co., Ltd. Ethanol was purchased from Shang hai Macklin Biochemical Technology Co., Ltd. Deionized water (DI water, 18.3 MΩ·cm) was used in all experiments.

2.2 Preparation of a-RuO_2

Typically, a-RuO_2 was prepared as follows: Firstly, 200 mg of $RuCl_3 \cdot xH_2O$ was dispersed in 100 mL of DI water. Then, 350 mg of KBr was dissolved into the above solution by ultrasonication for 20 min, and the solution turned dark red. Subsequently, the mixture was stirred vigorously at 60 ℃ until all the liquid evaporated. The resulting dark red powder was heated in an argon-filled tube furnace at 250 ℃ for 2 h at a heating rate of 6 $℃ \cdot min^{-1}$. Finally, the sample was thoroughly washed with ethanol and DI water, and dried at 60 ℃ overnight.

2.3 Characterizations

The morphology and structure of the catalysts were determined by various characterization techniques. Powder X-ray diffraction (XRD, PANalytical Empyrean, Netherlands) test was performed with a Cu K_α radiation source, and signals were acquired at 40 kV and 40 mA with a scan rate set to $10° \cdot min^{-1}$. X-ray photoelectron spectroscopy (XPS, KRATOS AXIS

Ultra DLD, England) using Al K_α as the X-ray source was employed to detect the chemical state of the samples. Scanning electron microscope (SEM, Zeiss Merlin Compact, Phenom Pro) and transmission electron microscope (TEM, JEM-2100, Japan) were used to examine the morphology and atomic arrangement of the samples, respectively.

2.4 Electrochemical Characterization

The catalyst was homogeneously mixed with Super P in a 2:1 mass ratio, and the mixed catalyst was dispersed in 5wt.% Nafion ethanol solution to prepare the catalyst ink (catalyst mass ratio of 5 mg·mL^{-1}). After ultrasonic dispersion for 30 min, 15 μL of homogeneous ink was dropped onto a pre-polished glassy carbon electrode (GCE, area: 0.07064 cm^2), which was then dried naturally at room temperature to obtain the working electrode with a loading of 0.4 mg·cm^{-2}. The electrochemical performance of the catalysts was studied in a three-electrode system, with a graphite rod as the counter electrode and Ag/AgCl as the reference electrode. Argon-saturated 0.5 mol·L^{-1} H_2SO_4 and 1.0 mol·L^{-1} KOH solutions were used as the electrolytes for acid HER and alkaline HER tests, respectively. All the applied potentials were converted through a reversible hydrogen electrode (RHE) with $E_{RHE} = E_{Ag/AgCl} + 0.059pH + 0.197$ V. Polarization curves were measured using linear scanning voltammetry (LSV) at a sweep rate of 5 mV·s^{-1} and corrected by 95% iR. The durability of the catalyst was evaluated using chronopotentiometry. Electrochemical impedance spectroscopic (EIS) data was measured with an applied 5 mV amplitude within the frequency range from 0.1 Hz to 10^5 Hz. The LSV was measured after 1000 CV cycles to further evaluate the stability of the catalyst.

2.5 Theoretical Calculation

All the calculations are performed using implemented in Quantum Espresso (QE) and density functional theory (DFT). The Projector Augmented Wave method (PAW) is used to describe the interactions. Perdew-Burke-Ernzerhof (PBE) function is used to deal with the relevant exchange energy of the system. To avoid pseudo-interactions between periodic images, a vacuum layer of 15 Å is added to the c-axis. A plane-wave energy cut off of 420 eV is used together with norm-conserving pseudopotentials. A 2 × 2 × 1 grid is used for Brillouin zone integration. Charge distribution of Ru-O configuration is investigated with Bader charge analysis. In all calculations, the convergence values of the total energy and force on each atom are 10^{-4} eV and 0.05 eV·Å^{-1}, respectively. The d-band center is calculated by

$$\varepsilon = \frac{\int_{-\infty}^{E_f} E \cdot \rho(E) dE}{\int_{-\infty}^{E_f} \rho(E) dE} \quad (1)$$

where ρ is the density of states, E is the energy relative to the Fermi level, and E_f is the Fermi level energy. The Gibbs free energy of the reactant conversion is calculated by correcting the DFT energy with the zero-point energy and entropy by

$$\Delta G = \Delta E + \Delta ZPE - T\Delta S \quad (2)$$

where S is the entropy value, T is the ambient temperature, ZPE is the zero-point energy, and E is the DFT total energy[18]. We use density functional perturbation theory to calculate the vibration frequency in order to further calculate the entropy and correct the zero-point energy.

3 Results and Discussion

Calcination temperature and time are crucial to controlling the crystallinity[19]. We synthesized a-RuO_2 with disordered Ru-O conformation by one-step low-temperature heat treatment, and compare with commercial crystalline RuO_2 (c-RuO_2). The structure and morphology of the catalysts were characterized by transmission electron microscopy (TEM) and scanning electron microscopy (SEM). As shown in Figure 1A-D, the average particle sizes of a-RuO_2 and c-RuO_2 are similar, indicating that the difference in catalytic activity mainly originates from the microstructure. The high-resolution transmission electron microscopic (HRTEM) images show a significant difference between the two catalysts. Figure 1E shows that c-RuO_2 has regular lattice stripes with a distance of 2.54 Å between adjacent stripes, corresponding to the (101) crystal plane of RuO_2. In contrast, a-RuO_2 exhibits a maze-like pattern with a random

distribution of all atoms (Figure 1F). The selected area electron diffraction (SAED) pattern with a diffuse halo-ring further confirms the amorphous character of a-RuO_2 (the inset of Figure 1F). Furthermore, the energy-dispersive X-ray spectroscopic (EDX) elemental mappings (Figure 1G and 1H) show the uniform distributions of Ru and O in a-RuO_2, indicating that the low-temperature heat-treated synthesized a-RuO_2 does not contain impurities such as Ru nanoparticles.

X-ray diffraction (XRD) test was first performed to study their crystal structures. Figure 2A shows the XRD spectra of a-RuO_2 and c-RuO_2. The three peaks at 27.8°, 35.0° and 54.2° are assigned to the (1 1 0), (1 0 1), and (2 1 1) faces of rutile crystalline RuO_2, respectively. These peaks were observed in commercial c-RuO_2, while a-RuO_2 showed only broad and weak peaks, indicating that a-RuO_2 does not form an ordered metal compound but presents an amorphous structure, which is consistent with the HRTEM results. In addition, we calculated the lattice spacing of c-RuO_2 via Bragg's law

$$2d\sin\theta = n\lambda \quad (3)$$

where θ is the angle between the incident ray and the reflecting surface, d is the lattice spacing, n is the number of reflection levels, and λ is the incident X-ray wavelength. The lattice spacing corresponding to the peak of c-RuO_2 at 35.0° is calculated to be 2.5 Å, which confirms that the crystal plane shown in Figure 1F is (1 0 1). Based on this, we chose the (1 0 1) crystal plane of c-RuO_2 as the exposed plane for HER simulations. ICP-OES tests were performed to determine the effect of amorphization on the ratio of catalyst elements (Table 1). Unlike c-RuO_2 where the elements are close to the theoretical ratio (Ru:O = 1:2), a-RuO_2 has less oxygen content, which may be due to calcination in the air resulting in the detachment of oxygen atoms and formation of oxygen vacancies in a-RuO_2.

X-ray photoelectron spectroscopy (XPS) was used to further identify the chemical states of a-RuO_2 before and after the alkaline HER test. The high-resolution XPS spectrum in Figure 2B is attributed to the superposition of Ru 3d and C 1s signals[20]. The peak at 284.6 eV can be assigned to the C-C or C-H bond, originating from exotic carbon contaminating. In addition, the low-energy double peaks at 281.5 eV and 286.1 eV showing Ru $3d_{5/2}$ are attributed to Ru^{4+} with $Ru^{x<4}$, while the peak at 282.3 eV originates from the satellite peak. Reference literature reports that pristine a-RuO_2 has higher energy than crystalline RuO_2,

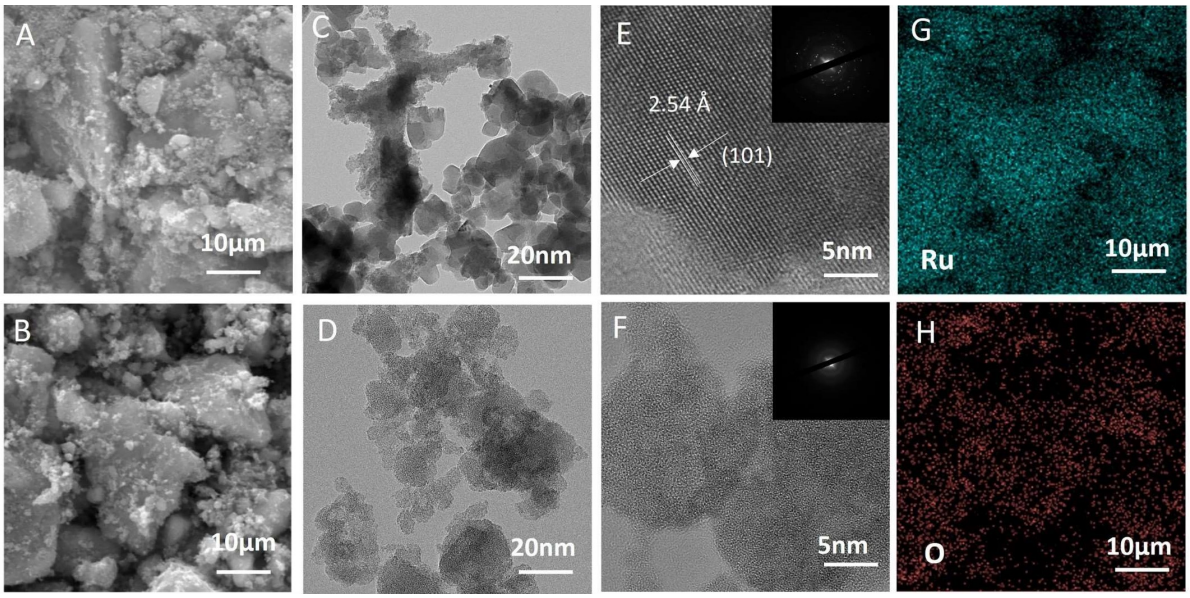

Figure 1 SEM images of (A) c-RuO_2 and (B) a-RuO_2. TEM images of (C) c-RuO_2 and (D) a-RuO_2. HRTEM images of (E) c-RuO_2 and (F) a-RuO_2. (G, H) Mapping images of a-RuO_2. (color on line)

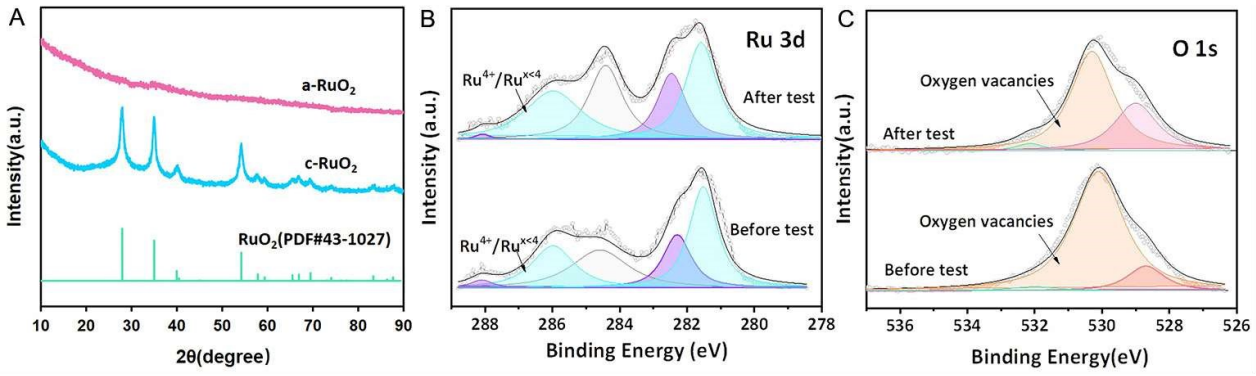

Figure 2 (A) XRD patterns of rutile RuO_2, c-RuO_2 and a-RuO_2. (B, C) High-resolution XPS Ru 3d and O 1s spectra of a-RuO_2 before and after HER test in alkaline media. (color on line)

Table 1 ICP-OES mass analysis results of a-RuO_2 and c-RuO_2 samples

Sample	$\frac{m_{Ru}/M_{Ru}}{m_{RuO_2}/M_{RuO_2}}$	$1-\frac{m_{Ru}/M_{Ru}}{m_{RuO_2}/M_{RuO_2}}$
a-RuO_2	34.3%	65.7%
c-RuO_2	33.1%	66.9%

implying that the structural disorder leads to the generation of electron-rich Ru[21]. After performing alkaline HER tests, the position of the Ru $3d_{5/2}$ peak hardly shifted, implying that HER tests did not affect the Ru oxidation state. The XPS spectra of O 1s are shown in Figure 2C, with peaks at 528.7, 530.1, and 531.8 eV corresponding to lattice oxygen (Ru-O), defective sites with low oxygen coordination and surface adsorbed hydroxyl species, respectively[22]. The primitive a-RuO_2 has a significant predominance of defective oxygen, stemming from the disordered Ru-O conformation, leading to an insufficient number of O coordination sites. After performing the alkaline HER test, the peak at 530.1 eV decreased slightly and increased at 528.7 and 531.8 eV. This is probably due to the self-healing of the amorphous catalyst and the incomplete detachment of the hydroxyl[23].

The electrocatalytic activity of HER was evaluated with a typical three-electrode system in 0.5 mol·L^{-1} H_2SO_4. The commercial 20wt% Pt/C was employed for comparison. The crystalline structure was modulated to explore the electrocatalytic performance. As depicted in Figure 3A, the commercial Pt/C exhibited excellent electrocatalytic activities. Except Pt/C electrocatalyst, a-RuO_2 shows a low onset overpotential of 67 mV (Figure 3A). Nevertheless, the onset overpotential of c-RuO_2 (105 mV) is larger than that of a-RuO_2. Furthermore, a-RuO_2 shows a small overpotential of 85 mV at a current density of 10 mA·cm^{-2}, lower than c-RuO_2 (155 mV). Notably, the Tafel slope of a-RuO_2 was assessed to be 45.4 mV·dec^{-1}, much lower than that of c-RuO_2 (84.6 mV·dec^{-1}) (Figure 3B). Figure 3C shows the electrocatalytic durability of a-RuO_2, evident from the current-time plot, indicating its superior long-term durability. Moreover, the polarization curves for the 1st and the 1000th cycles of a-RuO_2 are still superimposed, once again demonstrating its superior stability (Figure 3D). The HER reaction kinetics of electrocatalysts was studied by electrochemical impedance spectroscopy (EIS). The EIS plots prove that the charge-transfer resistance of a-RuO_2 was meaningfully weakened as compared with that of c-RuO_2 (Figure 3E). The preferable charge transfer system is a-RuO_2, which was attributed to the particular electronic structure of amorphous matrix

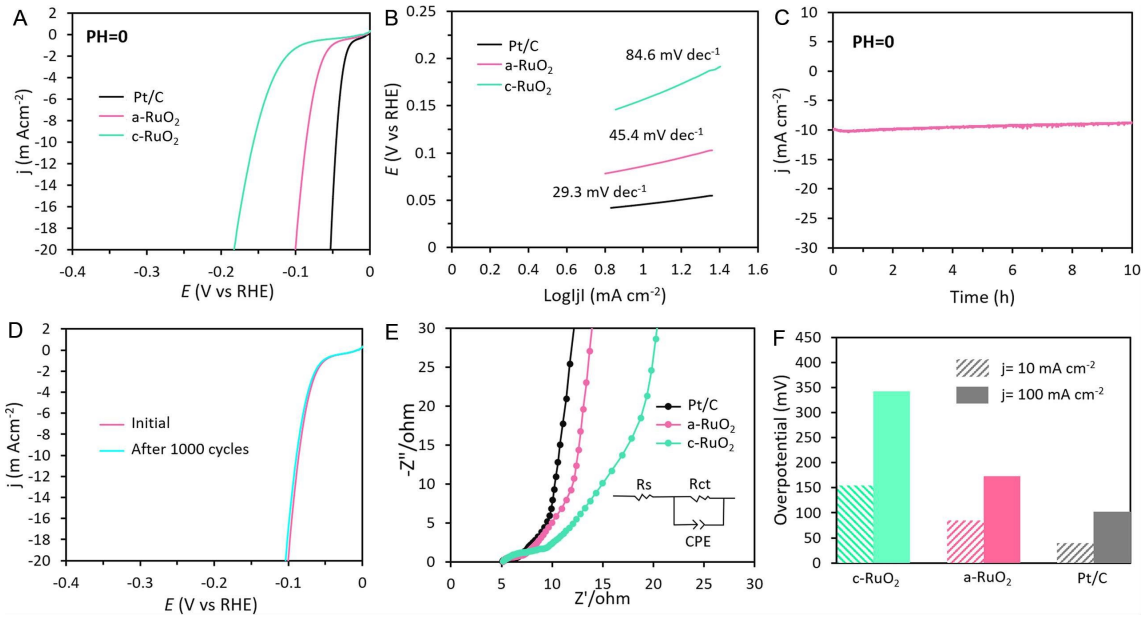

Figure 3 (A) LSV polarization curves of a-RuO_2, c-RuO_2, and commercial Pt/C in 0.5 mol·L^{-1} H_2SO_4. (B) Tafel plots for a-RuO_2, c-RuO_2, and Pt/C. (C) Current-time plot of a-RuO_2. (D) LSV curves of a-RuO_2 before and after 1000 cycles. (E) Nyquist plots of a-RuO_2, c-RuO_2, and Pt/C. The inset is analog circuit diagram. (F) The corresponding electrocatalysts overpotentials at 10 and 100 mA·cm^{-2}. (color on line)

and large interface surface between a-RuO_2 and solution, according with the remarkable HER performance. The intended overpotentials at both 10 and 100 mA·cm^{-2} are evaluated as depicted in Figure 3F. To arrive at 100 mA·cm^{-2}, the commercial Pt/C requires an overpotential of 102 mV, while a-RuO_2 and c-RuO_2 require 173 and 342 mV, respectively. The results show that amorphous catalysts exhibit the best catalytic performance at different current densities.

The electrocatalytic performance of the a-RuO_2 and c-RuO_2 was also investigated in 1 mol·L^{-1} KOH, and is compared with that of Pt/C, which exhibits a considerably smaller overpotential. Moreover, as shown in Figure 4A, a-RuO_2 reached 10 mA·cm^{-2} at an overpotential of 110 mV which is lower than that of c-RuO_2 (180 mV). Next, the HER reaction kinetics of these electrocatalysts were evaluated by fitting LSV curves according to the Tafel equation (Figure 4B). The slope in Tafel plot for a-RuO_2 is calculated to be 52.7 mV·dec^{-1}, much lower than that of c-RuO_2 (92.4 mV·dec^{-1}). Therefore, a-RuO_2 has a relatively fast kinetic profile in electrocatalytic reactions under alkaline conditions. The stability test of a-RuO_2 in 1 mol·L^{-1} KOH is depicted in current-time dependence to check the HER durability of the electrocatalysts further. As depicted in Figure 4C, the current-time dependence plots of the catalysts in the alkaline solution merely show damping of electrocatalytic performance. In addition, there is no visible gap of the electrocatalytic performance in the 1st and the 1000th cycles, indicating the favorable extended durability of a-RuO_2 for HER reaction (Figure 4D). As shown in Figure 4E, we also employed EIS to study HER reaction kinetics. Under the alkaline condition, Nyquist plots display that the charge transfer resistance of a-RuO_2 is significantly reduced confronted with c-RuO_2. Furthermore, a-RuO_2 reached 100 mA·cm^{-2} at a relatively small overpotential of 252 mV, which is lower than c-RuO_2 (391 mV) in the alkaline media (Figure 4F).

All electrochemical tests support that the disordered Ru-O conformation has significantly enhanced acidic and alkaline HER activities compared to the ordered coordination. Tafel plot has also shown a-RuO_2 to have a fast kinetic response, which may be attributed to the disordered conformation enhancing

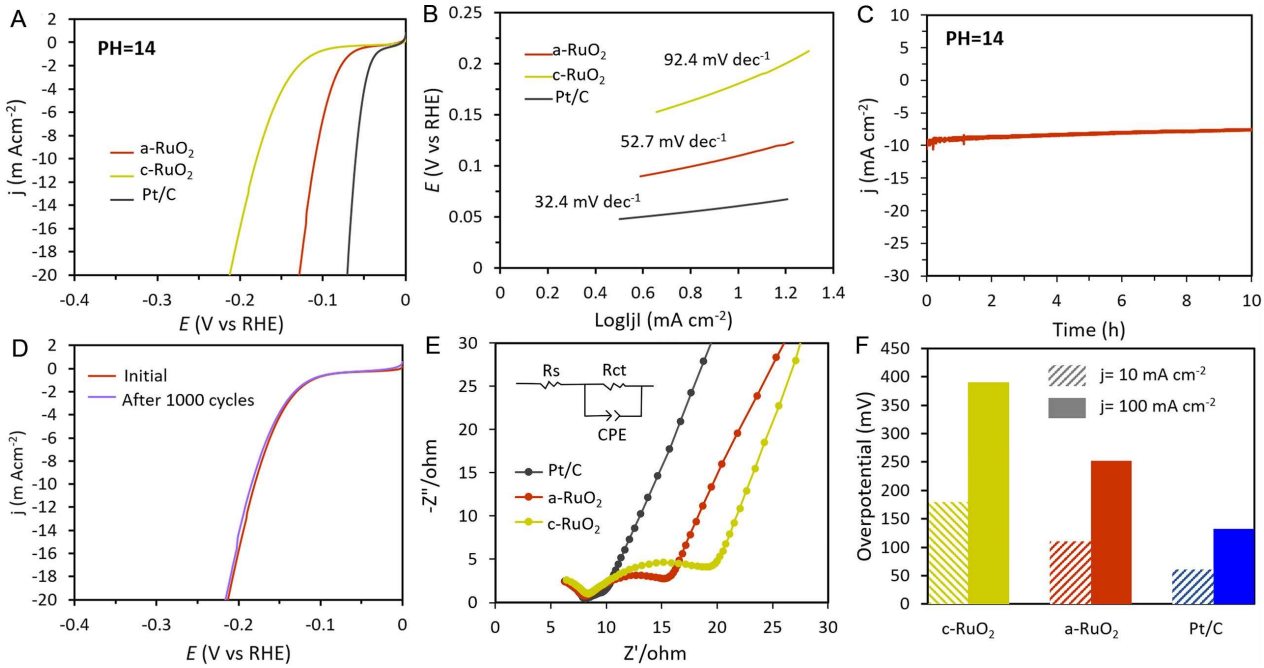

Figure 4 (A) LSV curves and (B) Tafel plots of a-RuO_2, c-RuO_2, and Pt/C in 1 mol·L^{-1} KOH. (C) Current-time plot of a-RuO_2 in 1 mol·L^{-1} KOH. (D) LSV curves of a-RuO_2 before and after 1000 cycles in 1 mol·L^{-1} KOH. (E) Nyquist plots of a-RuO_2, c-RuO_2, and Pt/C in 1 mol·L^{-1} KOH. The inset is analog circuit diagram (F) The corresponding overpotentials at 10 and 100 mA·cm^{-2} in 1 mol·L^{-1} KOH. (color on line)

the transport of the reactants and optimizing their adsorption on the catalyst surface. In this regard, a detailed simulation analysis is carried out later.

To further reveal the reason for the excellent electrocatalytic HER performance of a-RuO_2, we evaluated the catalytic mechanism of the disordered Ru-O conformation by DFT simulations and kinetic analysis. The differential charge densities of the two models are simulated. Figures 5A and 5B show that Ru in a-RuO_2 has diverse charge transfers compared to the uniform electron transfer in c-RuO_2. Specifically, the disordered Ru-O configuration with diverse spatial orientations and bond lengths triggers inhomogeneous space-charge interactions, leading to Ru exhibiting different charge accumulations and charge depletions. This diffusely heterogeneous charge distribution drives the generation of numerous highly active sites. Figures 5C and 5D also confirm that the disordered Ru-O distribution leads to dispersion of the charge density of Ru. To investigate the effect of Ru-O conformational ordering on the electronic structure, we calculate the spin-resolved density of states (DOS) for two samples. As shown in Figure 5E, the DOS of C-RuO_2 is sharp and localized due to the two-dimensional bonding in the layered structure of the crystal structure, while the DOS of A-RuO_2 is relatively broad and delocalized stemming from the distortion of the layered structure. In addition, a-RuO_2 shows a higher density of states at the Fermi energy level and thus has a higher electronic conductivity than c-RuO_2[24]. The state of Ru d orbital has a significant effect on the HER. The DOS plots of the Ru 4d bands are shown in Figures 5F and 5G. The calculated d-band centers of a-RuO_2 and c-RuO_2 are located at -2.91 eV and -1.45 eV, respectively. The lower d-band center of a-RuO_2 compared to c-RuO_2 indicates weaker adsorption of H, leading to easier H reformation on a-RuO_2 and promoting HER performance. In addition, the electron localization function (ELF) indicates that a-RuO_2 can achieve uniform electron tour in 3D space than c-RuO_2, which provides numerous electron transfer channels for HER

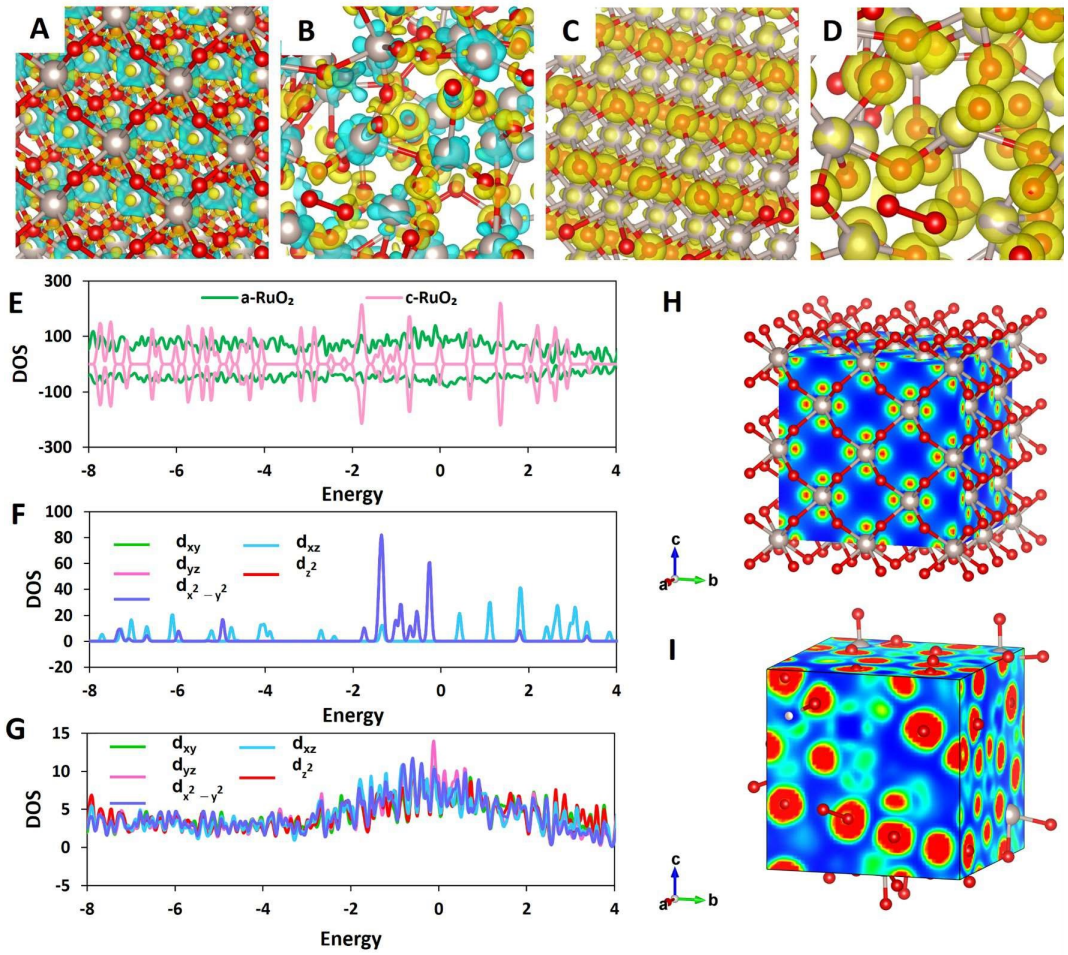

Figure 5 Differential charge density graphs of (A) c-RuO_2 and (B) a-RuO_2. Charge density graphs of (C) c-RuO_2 and (D) a-RuO_2. (E) Total density of states (TDOS) plots of c-RuO_2 and a-RuO_2. Ru 3d orbital projected density of states (PDOS) plots for (F) c-RuO_2 and (G) a-RuO_2. 3D ELF maps of (H) c-RuO_2 and (I) a-RuO_2. (color on line)

and facilitates the full expression of active sites in all directions of the catalyst (Figures 5H and 5I).

The Gibbs free energy of catalyst for hydrogen adsorption (ΔG_{H^*}) is an essential indicator for analyzing catalytic activity. A positive ΔG_{H^*} is detrimental to H* adsorption but beneficial to product desorption, while a negative ΔG_{H^*} is the opposite. In order to achieve excellent HER performance, the binding strength of H^+ to the catalytic surface should be moderate, so the ΔG_{H^*} of an ideal HER catalyst should be close to zero[25]. We investigated the adsorption energies of intermediate reactants on the c-RuO_2 (1 0 1) surface and the Ru atoms in charge depletion on a-RuO_2. Figures 6A and 6B show the free energy competition in acidic and alkaline media. H_2 is produced via the Volmer-Heyrovsky pathway ($H^+ + e^- + * \rightarrow H^*$; $H^* + H^+ + e^- \rightarrow H_2 + *$) in acidic media. The results show that c-RuO_2 adsorbs H too strongly and a-RuO_2 adsorbs H somewhat weakly, promoting the release of H_2 from the a-RuO_2 surface, indicating the best activity, which is consistent with the experimental electrochemical results. Moreover, in alkaline media, HER is usually achieved by three steps: H_2O (l) $\rightarrow$ H_2O^* $\rightarrow$ $OH^* + H^* \rightarrow OH^* + 1/2\ H_2$ (g)[26]. Therefore, in contrast to acidic HER, the energy profile of alkaline HER contains an investigation of the energy barrier of water dissociation. As shown in Figure 6B, a-RuO_2 exhibits the lowest Gibbs free energy for water molecules, ensuring sufficient H_2O^* for the subsequent HER. Notably, the decomposition of H_2O^* into

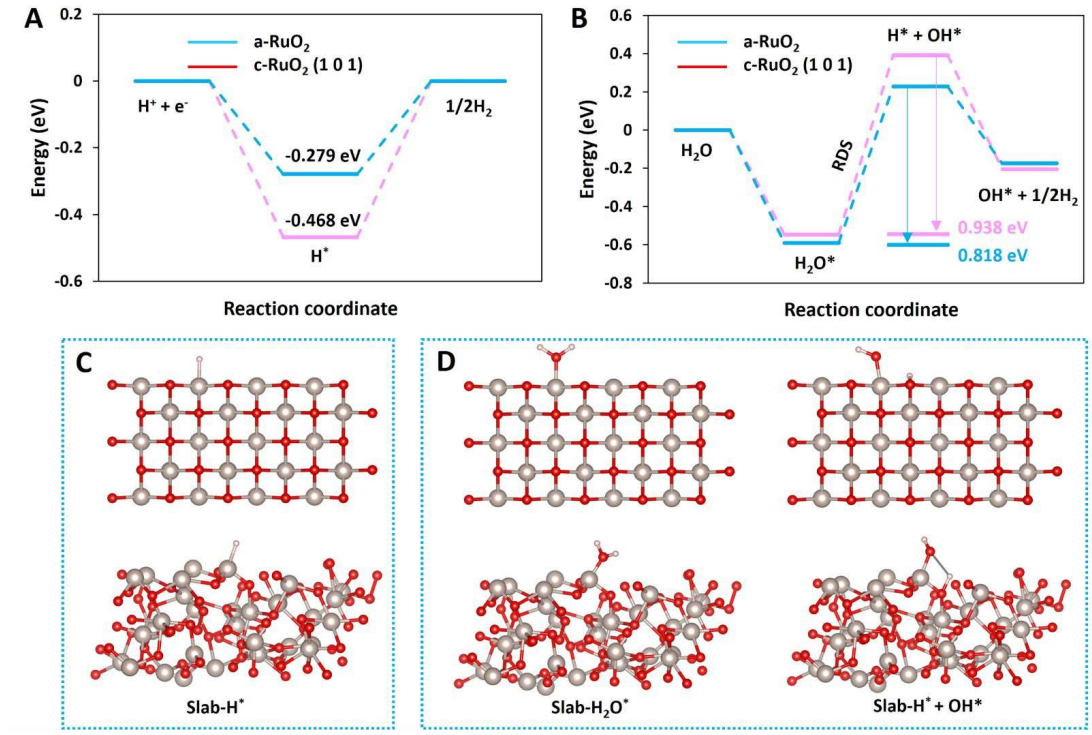

Figure 6 Calculated free energy diagrams of (A) acidic HER and (B) alkaline HER. (C) and (D) show the optimized structures of acidic and alkaline HER intermediate reactants adsorbed on the catalyst surface, respectively. (color on line)

OH* and H* has the largest Gibbs free energy change, representing the rate-determining step (RDS) of the alkaline HER[27]. Therefore, the magnitude of the absolute value of the free energy change from H_2O* to OH* + H* can reflect the HER activity of the catalyst. Obviously, a-RuO_2 has a smaller value of free energy change (0.818 eV) than c-RuO_2 (0.938 eV). This implies that the disordered Ru-O conformation can promote electrocatalytic hydrolysis and accelerate the RDS of alkaline HER. Figures 6C and 6D depict the optimized configurations of HER intermediate adsorbates on the two catalysts. Combining all the experimental results and theoretical calculations, we conclude that the disordered Ru-O conformation can regulate the charge accumulation and consumption at the active site of the catalyst, which in turn optimizes the d-band center and the affinity for the intermediate reactants. Ultimately, the structurally disordered a-RuO_2 exhibits significantly enhanced HER catalytic performance.

4 Conclusions

In conclusion, we developed amorphous a-RuO_2 catalyst with disordered Ru-O conformation. The fully exposed disordered structure gave a-RuO_2 a far superior HER performance than crystalline c-RuO_2, exhibiting HER activity close to that of commercial Pt/C in both alkaline and acidic media. Impressively, a low overpotential of 110 mV and a small Tafel slope of 52.7 mV·dec^{-1} were achieved in alkaline media at a geometric current density of 10 mA·cm^{-2}. The conformational relationship between microstructure and catalytic performance has been investigated with experimental tests and theoretical simulations. The homogeneous charge channels and high conductivity of the amorphous catalyst enable rapid charge transfer to either site. The disordered Ru-O conformation modulates the d-band center and affinity for intermediate reactants, thus, reducing the kinetic barriers to the HER process and achieving the optimal hydrogen production performance. This work provides new insight into efficient HER catalysis through phase engineering.

Acknowledgments

This work was supported by National Natural Science

Foundation of China (No. 22075063, No. U1932205, No. 22102041), Fundamental Research Funds for the Central Universities (FRFCU5710092520), Chinesisch-Deutschen Zentrum für Wissenschaftsförderung (M-0281), Natural Science Funds of Heilongjiang Province (No. ZD2019B001), Heilongjiang Touyan Team (HITTY-20190033), the Natural Science Fund for Distinguished Young Scholars of Chongqing (cstc-2021jcyj-jqX0003), "Young Scientist Studio" and Chongqing Research Institute of HIT.

References:

[1] Pei Y, Cheng Y, Chen J Y, Smith W, Dong P, Ajayan P M, Ye M X, Shen J F. Recent developments of transition metal phosphides as catalysts in the energy conversion-field[J]. J. Mater. Chem. A, 2018, 6(46): 23220-23243.

[2] Shi Y, Ma Z R, Xiao Y Y, Yin Y C, Huang W M, Huang Z C, Zheng Y Z, Mu F Y, Huang R, Shi G Y, Sun Y Y, Xia X H, Chen W. Electronic metal-support interaction modulates single-atom platinum catalysis for hydrogen evolution reaction[J]. Nat. Commun., 2021, 12(1): 3021.

[3] Li L G, Wang P T, Shao Q, Huang X Q. Metallic nanostructures with low dimensionality for electrochemical water splitting[J]. Chem. Soc. Rev., 2020, 49(10): 3072-3106.

[4] Jiao Y, Zheng Y, Jaroniec M T, Qiao S Z. Design of electrocatalysts for oxygen- and hydrogen-involving energy conversion reactions[J]. Chem. Soc. Rev., 2015, 44(8): 2060-2086.

[5] Zhao D, Sun K A, Cheong W C, Zheng L R, Zhang C, Liu S J, Cao X, Wu K L, Pan Y, Zhuang Z W, Hu B T, Wang D S, Peng Q, Chen C, Li Y D. Synergistically interactive pyridinic-n-MoP sites: Identified active centers for enhanced hydrogen evolution in alkaline solution[J]. Angew. Chem. Int. Ed., 2020, 59(23): 8982-8990.

[6] Xia J W, Volokh M, Peng G M, Fu Y S, Wang X, Shalom M. Low-cost porous ruthenium layer deposited on nickel foam as a highly active universal-pH electrocatalyst for the hydrogen evolution reaction[J]. ChemSusChem, 2019, 12 (12): 2780-2787.

[7] Zheng Y, Jiao Y, Zhu Y H, Li L H, Han Y, Chen Y, Jaroniec M, Qiao S Z. High electrocatalytic hydrogen evolution activity of an anomalous ruthenium catalyst[J]. J. Am. Chem. Soc., 2016, 138(49): 16174-16181.

[8] Wang Y, Kong B, Zhao D Y, Wang H T, Selomulya C. Strategies for developing transition metal phosphides as heterogeneous electrocatalysts for water splitting[J]. Nano Today, 2017, 15: 26-55.

[9] Han Z, Zhang R L, Duan J J, Wang A J, Zhang Q L, Huang H, Feng J J. Platinum-rhodium alloyed dendritic nanoassemblies: An all-pH efficient and stable electrocatalyst for hydrogen evolution reaction[J]. Int. J. Hydrogen Energy, 2020, 45(11): 6110-6119.

[10] Hu J, Zhang C X, Jiang L, Lin H, An Y M, Zhou D, Leung M K H, Yang S H. Nanohybridization of MoS_2 with layered double hydroxides efficiently synergizes the hydrogen evolution in alkaline media[J]. Joule, 2017, 1(2): 383-393.

[11] Cheng C, Shah S S A, Najam T, Qi X Q, Wei Z D. Improving the electrocatalytic activity for hydrogen evolution reaction by lowering the electrochemical impedance of RuO_2/Ni-P[J]. Electrochim. Acta, 2018, 260: 358-364.

[12] Liu J L, Zheng Y, Jiao Y, Wang Z Y, Lu Z G, Vasileff A, Qiao S Z. NiO as a bifunctional promoter for RuO_2 toward superior overall water splitting[J]. Small, 2018, 14(16): 1704073.

[13] Xia Y J, Wu W Q, Wang H, Rao S L, Zhang F Y, Zou G F. Amorphous RuS_2 electrocatalyst with optimized active sites for hydrogen evolution[J]. Nanotechnology, 2020, 31 (14): 145401.

[14] Shin S, Jin Z, Kwon D H, Bose R, Min Y S. High turnover frequency of hydrogen evolution reaction on amorphous MoS_2 thin film directly grown by atomic layer deposition [J]. Langmuir, 2015, 31(3): 1196-1202.

[15] Cao D, Wang J Y, Xu H X, Cheng D J. Growth of highly active amorphous RuCu nanosheets on Cu nanotubes for the hydrogen evolution reaction in wide pH values [J]. Small, 2020, 16(37): 2000924.

[16] Wang J, Hu J, Niu S Q, Li S W, Du Y C, Xu P. Crystalline-amorphous $Ni_2P_4O_{12}$/$NiMoO_x$ nanoarrays for alkaline water electrolysis: Enhanced catalytic activity via *in situ* surface reconstruction[J]. Small, 2022, 18(10): 2105972.

[17] Arenal R, Lopez-Bezanilla A. *In situ* formation of carbon nanotubes encapsulated within boron nitride nanotubes via electron irradiation[J]. ACS Nano, 2014, 8(8): 8419-8425.

[18] Norskov J K, Bligaard T, Logadottir A, Kitchin J R, Chen J G, Pandelov S, Norskov J K. Trends in the exchange current for hydrogen evolution[J]. J. Electrochem. Soc., 2005, 152(3): J23-J26.

[19] Wu H M, Feng C Q, Zhang L, Zhang J J, Wilkinson D P. Non-noble metal electrocatalysts for the hydrogen evolution reaction in water electrolysis[J]. Electrochem. Energy Rev., 2021, 4(3): 473-507.

[20] Zhang L J, Jang H, Liu H H, Kim M G, Yang D J, Liu S G, Liu X E, Cho J. Sodium-decorated amorphous/crys-

talline RuO_2 with rich oxygen vacancies: A robust pH-universal oxygen evolution electrocatalyst [J]. Angew. Chem. Int. Ed., 2021, 60(34): 18821-18829.

[21] Rochefort D, Dabo P, Guay D, Sherwood P M A. XPS investigations of thermally prepared RuO_2 electrodes in reductive conditions[J]. Electrochim. Acta, 2003, 48(28): 4245-4252.

[22] Wang Y T, Li H J, Zhou W, Zhang X, Zhang B, Yu Y F. Structurally disordered RuO_2 nanosheets with rich oxygen vacancies for enhanced nitrate electroreduction to ammonia[J]. Angew. Chem. Int. Ed., 2022, 61(19): e202202604.

[23] Zhang Y J, Xu Z F, Li G Y, Huang X J, Hao W C, Bi Y P. Direct observation of oxygen vacancy self-healing on TiO_2 photocatalysts for solar water splitting[J]. Angew. Chem. Int. Ed., 2019, 58(40): 14229-14233.

[24] Johannes M D, Stux A M, Swider-Lyons K E. Electronic structure and properties of Li-insertion materials: Li_2RuO_3 and RuO_2[J]. Phys. Rev. B, 2008, 77(7): 075124.

[25] Qiu H J, Ito Y, Cong W T, Tan Y W, Liu P, Hirata A, Fujita T, Tang Z, Chen M W. Nanoporous graphene with single-atom nickel dopants: An efficient and stable catalyst for electrochemical hydrogen production[J]. Angew. Chem. Int. Ed., 2015, 54(47): 14031-14035.

[26] Huang H W, Jung H, Li S F, Kim S, Han J W, Lee J. Activation of inert copper for significantly enhanced hydrogen evolution behaviors by trace ruthenium doping [J]. Nano Energy, 2022, 92: 106763.

[27] Shang H S, Zhao Z H, Pei J J, Jiang Z L, Zhou D N, Li A, Dong J C, An P F, Zheng L R, Chen W X. Dynamic evolution of isolated Ru-FeP atomic interface sites for promoting the electrochemical hydrogen evolution reaction[J]. J. Mater. Chem. A, 2020, 8(43): 22607-22612.

无序 Ru-O 构型对电化学析氢催化性能研究

孙 雪[1,2],宋亚杰[1,2],李仁龙[1],王家钧[1,2*]

(1. 哈尔滨工业大学, 工信部新能源转换与存储关键材料技术重点实验室, 黑龙江 哈尔滨,150001;
2. 哈尔滨工业大学重庆研究院, 四川 重庆, 401135)

摘要: 相工程被认为是调节催化剂电子结构和催化活性的有效方法。非晶材料的无序构型允许表面电子结构的灵活重整，显示出其作为析氢反应（HER）催化剂的吸引力。在此，我们设计并开发了一种具有无序 Ru-O 构型的非晶催化剂（a-RuO_2）。结合先进的电镜技术和详细的电化学测试，建立了 Ru-O 有序性与 HER 性能的构效关系。具体来说，无序的 Ru-O 配位显著增强了酸性和碱性 HER 中的催化活性，最终使经济性更高的 a-RuO_2 催化性能接近商业 Pt/C。此外，在 10 mA·cm^{-2} 下进行 10 h 电流-时间（*i*-*t*）测试后，a-RuO_2 表现出极好的稳定性。进一步的理论模拟显示 a-RuO_2 较低的 d 带中心和优化的电子输运调制了活性位点对中间反应物的吸附强度，促进了 HER 动力学。这项工作为通过相工程探索高活性 HER 催化剂提供了新的观点。

关键词: 相工程; 电化学析氢; 非晶催化剂; 电子结构